Supplement of

Ether and ester formation from Peroxy Radical Recombination: A qualitative reaction channel analysis

Lauri Franzon[a], Marie Camredon[b], Richard Valorso[b], Bernard Aumont[b], and Theo Kurtén[a]

[a]Department of Chemistry, University of Helsinki, P.O. Box 55 (A.I. Virtasen aukio 1), 00014 Helsinki, Finland
[b]Univ Paris Est Creteil and Université Paris Cité, CNRS, LISA, F-94010 Créteil, France

Correspondence: Lauri Franzon (lauri.franzon@helsinki.fi)

Contents

S1 Parametrization of the Effective Hydrogen Bond Number

When looking for an ideal HBN parametrization to filter out weakly bounded ^{3}(RO...OR) complexes, we must first determine a limit for weak binding. As we have established that the ISC rate forming the ROOR product is often of order $k_{ISC} \approx 10^9 \text{ s}^{-1}$, a suitable choice would be to pick the binding energy corresponding the the dissociation rate $k_d \approx 10^8 \text{ s}^{-1}$. The relationship between the energies and the dissociation rates calculated in our previous work (Franzon, 2023) is presented in Figure S1.
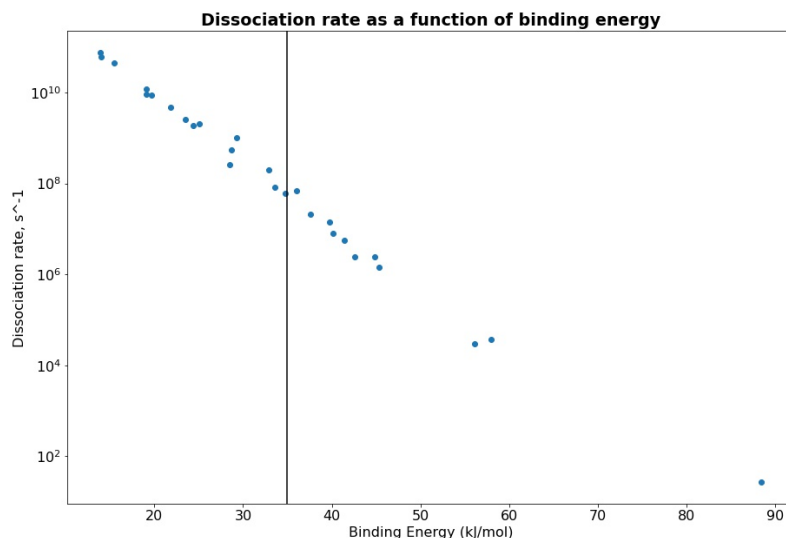
Figure S1. Dissociation rates calculated in Franzon (2023) as a function of complex binding energy. A vertical line is drawn at 35 kJ/mol to demonstrate that this is where the $10 k_d < k_{ISC} = 10^9 \text{ s}^{-1}$.

As we have noted previously, C-H bonds have shown weak H-bond donor behaviour in computational studies on ^{3}(RO...OR) complexes. The 'partial H-bond donor value' ascribed to these bonds was determined by calculating the HBN values for all 31 ^{3}(RO...OR) from Hasan (2023) using various values for the CH bond and searching for the best correlation between the binding energy and the HBN. The results are presented in Figure S2 and in Table S1. As seen in the figure, the partial donor value of 0.04 gave the best correlation, and this was thus used in the code.
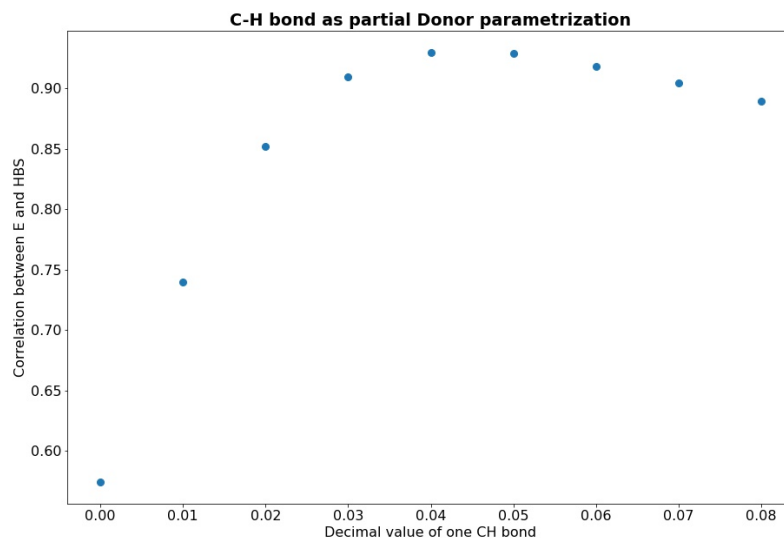
Figure S2. Correlation between effective H-Bond number and binding energies with various fractional donor values assigned to the C-H bonds.

Of course, this approach of estimating the binding energy using only the H-bonding properties ignores the impact of molecular geometry. A hint of the impact of this omission is seen in Figure S3. A good fit of the complex binding energy as a function of HBN is only received if one removes the molecules with multiple stereoisomers from the data. In other words, a good estimate of the binding energy is only received if the molecules are relatively small and unconstrained by their geometry. However, molecules for which this geometry matters are likely to be larger, with more than enough H-bonding groups to make it over the threshold of inclusion. If this assumption is correct, the deficiencies of this H-bonding model will not matter, as we are only using it to rule out too weakly bonded complexes. In the linear fit presented in Figure S3b the binding energy of 35 kJ/mol corresponds to the HBN value of 1.75. This value was thus used as a cutoff in the H-bond filter of the GECKO-AP code.

$$HBN_{\alpha,\beta} = n_{\mathrm{D},\alpha} \cdot n_{\mathrm{A},\beta} + n_{\mathrm{D},\beta} \cdot n_{\mathrm{A},\alpha} \tag{1}$$
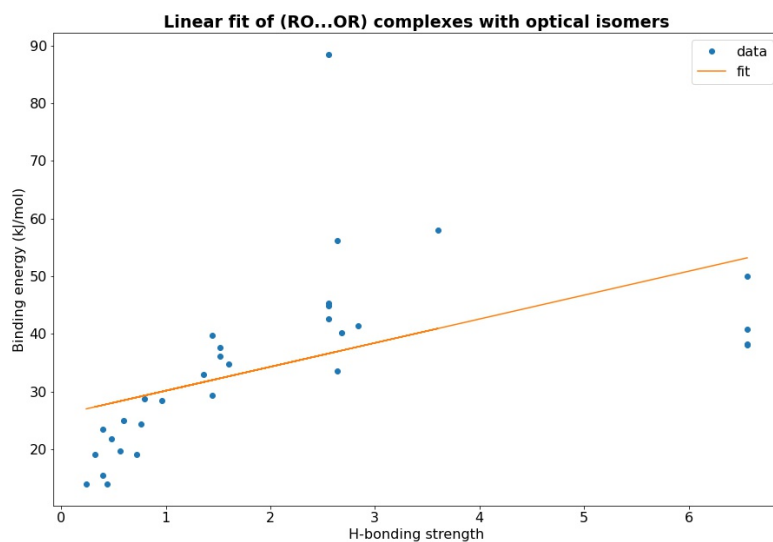
(a)
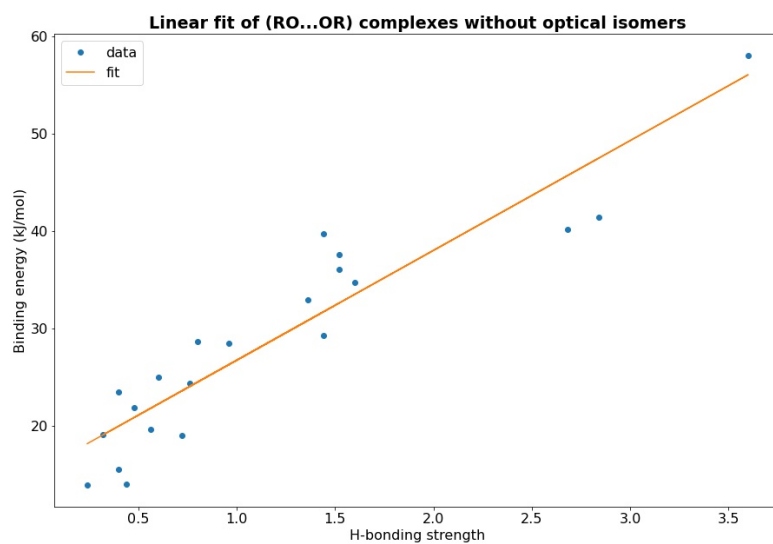
(b)

Figure S3. Linear fits of the $^{3}(\text{RO}\ldots\text{OR})$ binding energy as a function of the effective H-bond number. In (a), all of the complexes from Hasan (2023), whereas in (b), the complexes with multiple stereoisomers have been removed. The fit coefficients are $R^2 = 0.279$ and $R^2 = 0.864$, respectively.

Complex	$\Delta E \frac{\text{kJ}}{\text{mol}}$	$\ln k_d$	$n_{\text{CH},\alpha}$	$n_{D,\alpha}$	$n_{A,\alpha}$	$n_{\text{CH},\beta}$	$n_{D,\beta}$	$n_{A,\beta}$	HBN
(MetO)$_2$	13.89	10.88	3	0	1	3	0	1	0.24
(EtO)$_2$	23.46	9.41	5	0	1	5	0	1	0.4
(ProO)$_2$	19.65	9.95	7	0	1	7	0	1	0.56
(AceO)$_2$	28.68	8.73	5	0	2	5	0	2	0.8
(ButO)$_2$	19.03	9.96	9	0	1	9	0	1	0.72
R,R-(BuOHO)$_2$	56.15	4.47	8	1	1	8	1	1	2.64
R,S-(BuOHO)$_2$	33.57	7.91	8	1	1	8	1	1	2.64
(PrNO$_3$)$_2$	28.48	8.40	6	0	2	6	0	2	0.96
R-alk,R-nitr-α-pin	44.81	6.38	16	0	2	16	0	2	2.56
R-alk,S-nitr-α-pin	42.59	6.39	16	0	2	16	0	2	2.56
S-alk,R-nitr-α-pin	88.45	1.43	16	0	2	16	0	2	2.56
S-alk,S-nitr-α-pin	45.31	6.16	16	0	2	16	0	2	2.56
S-alk,R-hydr-α-pin	38.24	-[a]	16	1	2	16	1	2	6.56
R-alk,S-hydr-α-pin	38.07	-[a]	16	1	2	16	1	2	6.56
S-alk,S-hydr-α-pin	40.84	-[a]	16	1	2	16	1	2	6.56
R-alk,R-hydr-α-pin	40.04	-[a]	16	1	2	16	1	2	6.56
(α-pin-O$_3$$-$RO)$_2$[b]	58	4.57	15	0	3	15	0	3	3.6
MetO-EtO	19.12	10.08	3	0	1	5	0	1	0.32
MetO-ProO	15.48	10.65	3	0	1	7	0	1	0.4
MetO-AceO	13.97	10.78	3	0	1	5	0	2	0.44
MetO-ProOHO	32.93	8.30	3	0	1	6	1	1	1.36
MetO-BuOHO	29.25	9.01	3	0	1	8	1	1	1.44
EtO-ProO	21.84	9.67	5	0	1	7	0	1	0.48
EtO-AceO	25.02	9.31	5	0	1	5	0	2	0.6
EtO-ProOHO	39.71	7.16	5	0	1	6	1	1	1.44
EtO-BuOHO	36.07	7.83	5	0	1	8	1	1	1.52
ProO-AceO	24.39	9.28	7	0	1	5	0	2	0.76
ProO-ProOHO	37.57	7.32	7	0	1	6	1	1	1.52
ProO-BuOHO	34.75	7.78	7	0	1	8	1	1	1.6
AceO-ProOHO	40.12	6.90	5	0	2	6	1	1	2.68
AceO-BuOHO	41.42	6.75	5	0	2	8	1	1	2.84

Table S1. Dissociation rates, binding energies, and HBN calculations for the ^{3}(RO$\ldots$OR) complexes from (Hasan, 2023). [a] The dissociation rates were never calculated by Franzon (2023), but we can likely assume that they would be lower than 10^8 s^{-1} by extrapolation from observed trends. [b] From Peräkylä et al. (2023).

S2   Correcting Recombination Yields for RC(O)O$_2$ H-shift Rates

As described in Sect. 2.1.2 of the main text, pairs of RO$_2$ are filtered by their recombination yields y, which are determined from $k_{\mathrm{RO_2RO_2}}$ rate coefficients corrected using the rates of the competing bimolecular reactions. Correcting the yields using the rates of competing *unimolecular* reactions is harder, as GECKO-A does not support RO$_2$ H-shift reactions (Often referred to as autoxidation, as this immediately results in O$_2$ addition to the product radical (Bianchi et al., 2019)) at the time of writing. These are known to be especially fast for RC(O)O$_2$ (Vereecken and Nozière, 2020; Seal et al., 2023), which incidentally also have rapid recombination rates with virtually all other RO$_2$'s (Jenkin et al., 2019). Accounting for the effect of unimolecular decay on the RC(O)O$_2$ recombination yields is thus especially important, as these reactions will otherwise be over-represented in our data. The impact that the autoxidation rate has on the recombination yield for RC(O)O$_2$'s ($y_{\mathrm{RO_2RO_2},9}$) is modelled using Eq. 2 and compared to the recombination yields of the three next RO$_2$ classes for reference in Figure S4. As seen in the figure, an autoxidation rate of $0.1\ \mathrm{s}^{-1}$ depresses $y_{\mathrm{RO_2RO_2},9}$ below $y_{\mathrm{RO_2RO_2},8}$, and a rate of $1\ \mathrm{s}^{-1}$ depresses it below $y_{\mathrm{RO_2RO_2},7}$, but even if if this is the case, RO$_2$ + RC(O)O$_2$ reactions will still be among the more important RO$_2$ + RO$_2$ reactions.

$$y_{\mathrm{RO_2RO_2}} = \frac{k_{\mathrm{RO_2RO_2}}[\mathrm{RO_2}]^2}{k_{\mathrm{RO_2RO_2}}[\mathrm{RO_2}]^2 + k_{auto}[\mathrm{RO_2}] + \sum_i^5 k_i[\mathrm{Ox}]_i[\mathrm{RO_2}]} \tag{2}$$

Figure S4. The impact that different RC(O)O$_2$ autoxidation rates have on $y_{\mathrm{RO_2RO_2},9}$ relative to $y_{\mathrm{RO_2RO_2},8}$, $y_{\mathrm{RO_2RO_2},7}$ and $y_{\mathrm{RO_2RO_2},6}$. The yields are calculated assuming the representative intermediate concentrations $[\mathrm{NO}] = [\mathrm{NO_2}] = 2 \cdot 10^9$ molecule cm^{-3} (100 ppt), $[\mathrm{NO_3}] = 10^8$ molecule cm^{-3}, $[\mathrm{OH}] = 10^6$ molecule cm^{-3}, $[\mathrm{HO_2}] = 10^7$ molecule cm^{-3}.

Next, we need to evaluate how fast the $RC(O)O_2$ autoxidation rates actually are relative to the bimolecular reactions. This information is presented in Table S2, adapted from Seal et al. (2023). According to this computational study, autoxidation rates of simple $RC(O)O_2$ with four or more carbons are typically on the order of 0.1 s^{-1}. Based on earlier computational results, (Rissanen et al., 2014) these autoxidation rates can also be as high as 3.8 s^{-1} or 7.5 s^{-1} for acidic H atoms at ideal spans. However, as GECKO-A currently lacks a general autoxidation rate calculator, the approach taken for this work was to assume an uniform $RC(O)O_2$ autodixation rate of 1 s^{-1}, which sits in the upper-limit range for generic $RC(O)O_2$ autoxidation.

$RC(O)O_2$	Total	Approx
$MetC(O)O_2$	$7.3 \cdot 10^{-8}$	0
$EtC(O)O_2$	$9.0 \cdot 10^{-5}$	0
$PropC(O)O_2$	$1.0 \cdot 10^{-2}$	0.01
$ButC(O)O_2$	$6.9 \cdot 10^{-2}$	0.1
$PentC(O)O_2$	$2.0 \cdot 10^{-1}$	0.5
$HexC(O)O_2$	$4.2 \cdot 10^{-1}$	1
$SepC(O)O_2$	$2.5 \cdot 10^{-1}$	1
$OctC(O)O_2$	$4.5 \cdot 10^{-1}$	1

Table S2. The total autoxidation rate of simple acyl peroxy radicals as calculated by Seal et al. (2023). These rates are sums of the span-specific 1,n-H-shift rates presented in the original source.

An exception was made for the simplest and most common acyl peroxy radical, $MetC(O)O_2$, as this compound has a non-existent autoxidation rate (See Table S2) and a high ambient tropospheric concentration. (Villenave et al., 1998) Taken together, these facts imply that $MetC(O)O_2$ is the most likely RO_2 recombination partner for many radicals with otherwise slow $RO_2 + RO_2$ rates, justifying a special treatment in the rate filtering code. The values used for the recombination rate and yield correction factor are presented in Table S3.

Pair	Rate ($\frac{cm^3}{molecule\ s}$)	f_α
$RC(O)O_2 + RO_2$	$1.1 \cdot 10^{-11}$	0.035
$RC(O)O_2 + RC(O)O_2$	$1.4 \cdot 10^{-11}$	0.035
$MetC(O)O_2 + RO_2$	$1.1 \cdot 10^{-11}$	0.56
$MetC(O)O_2 + MetC(O)O_2$	$1.6 \cdot 10^{-11a}$	0.56
$MetC(O)O_2 + RC(O)O_2$	$1.4 \cdot 10^{-11}$	0.035

Table S3. Autoxidation-corrected recombination yield values for $RC(O)O_2$ reactions and uncorrected values for $MetC(O)O_2$ reactions.
[a] IUPAC task group recommendation.

60 S3 Computations on α-NO$_2$ ejection reaction

As the occurrence or non-occurrence of the α-NO$_2$ ejection reaction in the ^{3}(RO$\ldots$OR) complex proved to be of interest for accretion product inhibition (See Sect. 3.3 in the main text), the exact reaction rate of the reaction is a crucial detail. Thus the rate was computed for a set of four reference systems: CH$_2$(NO$_2$)O$\cdot$, CH$_3$CH(NO$_2$)O$\cdot$, (CH$_3$)$_2$C(NO$_2$)O$\cdot$, and CH$_2$=CH(CH$_3$)C(NO$_2$)O$\cdot$. The first of these is practically never important in the atmosphere, but as it is the simplest possible
65 α-NO$_2$ RO its result can be treated as a good reference rate for the importance of substituent effects relative to CH$_3$CH(NO$_2$)O$\cdot$ and (CH$_3$)$_2$C(NO$_2$)O$\cdot$, which are the more relevant simple α-NO$_2$ systems. CH$_2$=CHC(NO$_2$)O$\cdot$CH$_3$ was included as a fourth model system as the α-C=C substituent is fairly common for these radicals (19 out of 49 α-NO$_2$ RO$_2$ in the DTA dataset) owing to the fact that these radicals are derived from aromatic oxidation. This substituent is also known to speed up RO β-scissions. (Vereecken and Peeters, 2009)

70

All calculations were performed using the ORCA 5.0.4 program. Neese (2022) The molecular geometries and transition state saddle points were calculated using the ωB97X-D3 density functional (Lin et al., 2013) and the jun-cc-pV(T+d)Z basis set (Papajak et al., 2011). Full conformer searches were performed for both the reactants and transition states using CREST, (Pracht et al., 2020) and the reaction rates were calculated using Multi-Conformer Transition State Theory: (Møller et al., 2016)

$$75 \quad k_{MC-TST} = \frac{k_B T}{h} \frac{\sum_i^{n_{TS}} \kappa_i \mathrm{e}^{-\frac{G_i^\ddagger}{k_B T}}}{\sum_j^{n_R} \mathrm{e}^{-\frac{G_j}{k_B T}}} \tag{3}$$

where n_{TS} is the number of transition states found for the reaction, $G_i^\ddagger$ is the Gibbs free energy difference between the transition state and the global minimum reactant conformer, and κ_i is a tunneling coefficient calculated individually for each transition state. n_R is the number of reactant conformers and G_j is the Gibbs free energy difference of the reactant conformer relative to the global minimum, and k_B is the Boltzmann constant, h is the Planck constant, and T is the temperature. The
80 equation is rearranged somewhat from the original source to better accommodate the fact that the ORCA output gives free energy and entropy values (with low frequencies corrected using the Grimme Quasi-Harmonic approximation, Grimme (2012)) but not thermodynamic partition functions. The tunneling coefficients κ_i were calculated using the Eckart approach (Eckart, 1930; Johnston and Heicklen, 1962), using the Zero-point corrected energies of the reactant, transition state and product, where the latter was received by performing an Intrinsic Reaction Coordinate (Ishida et al., 1977) at the B3LYP/def2-SVP level of
85 theory (Stephens et al., 1994) and optimizing the resulting weakly bounded RC=O + $\cdot$NO$_2$ complex at the ωB97X-D3/jun-cc-pV(T+d)Z level. Conformer searches were not performed on the C=O + NO$_2$ product complex, as conformer differences in the reactant and TS were mainly caused by rotation of the breaking C-N bond. Thus, for the CH$_2$=CHC=OCH$_3$ + NO$_2$ system only the two conformers arising from the $\angle$(C=O, C=C) angle were considered, and for the other systems all TS were assumed to connect to the same product complex conformer. The results of the calculations are presented separately for each
90 of the found transition states in Table S4.

	$E_i^\ddagger$ ($\frac{\text{kJ}}{\text{mol}}$)	$G_i^\ddagger$ ($\frac{\text{kJ}}{\text{mol}}$)	ω_i (cm^{-1})	κ_i	k_i (s^{-1})	k_{MC-TST} (s^{-1})	ΔH ($\frac{\text{kJ}}{\text{mol}}$)
CH$_2$(NO$_2$)O·	27.16	26.90	-1067.74	3.39	$4.07 \cdot 10^8$	$4.07 \cdot 10^8$	-73.02
CH$_3$CH(NO$_2$)O· (TS 1)	21.99	21.58	-1048.09	3.06	$3.15 \cdot 10^9$		
CH$_3$CH(NO$_2$)O· (TS 2)	23.88	23.43	-1254.55	5.01	$2.45 \cdot 10^9$	$2.97 \cdot 10^9$	-94.26
(CH$_3$)$_2$C(NO$_2$)O· (TS 1)	20.01	20.12	-1264.69	4.63	$8.58 \cdot 10^9$		
(CH$_3$)$_2$C(NO$_2$)O· (TS 2)	15.95	20.55	-1264.24	4.07	$6.35 \cdot 10^9$	$1.41 \cdot 10^{10}$	-108.82
CH$_2$=CHC(NO$_2$)O·CH$_3$ (TS 1)	15.14	15.14	-1128.60	3.12	$4.32 \cdot 10^{10}$		
CH$_2$=CHC(NO$_2$)O·CH$_3$ (TS 2)	11.77	16.14	-1138.24	2.84	$2.63 \cdot 10^{10}$		
CH$_2$=CHC(NO$_2$)O·CH$_3$ (TS 3)	14.27	18.20	-1158.70	3.19	$1.29 \cdot 10^{10}$		
CH$_2$=CHC(NO$_2$)O·CH$_3$ (TS 4)	16.38	18.44	-1235.82	3.90	$1.43 \cdot 10^{10}$	$5.34 \cdot 10^{10}$	-120.16

Table S4. ωB97X-D3/jun-cc-pV(T+d)Z level computational results for the kinetics of α-NO$_2$ ejection from alkoxy radicals at $T = 298.15$ K. The TS are numbered from lowest to highest $G_i^\ddagger$. $E_i^\ddagger$ is the zero-point corrected activation barrier of each transition state relative to the reactant conformer that connects to it (In other words, the forward barrier value used in the Eckart tunneling coefficient calculation). ω_i is the imaginary vibrational frequency of the TS mode, and ΔH is the heat of the reaction.

Based on the results in Table S4, the α-NO$_2$ ejection is not quite as fast as the 'arbitrarily high' 10^{12} s^{-1} assigned to it by GECKO-A. Nevertheless the calculated MC-TST rates suggest that the reaction is indeed fast enough to sit firmly inside the 'competitive in-complex' range. Furthermore, for the (CH$_3$)$_2$C(NO$_2$)O· and CH$_2$=CHC(NO$_2$)O·CH$_3$ systems the rate is rapid enough to very likely be the dominant ^{3}(RO…OR) reaction channel in most cases, barring complexes with exceptionally fast ISC rates or extremely fast Exo-β-scission rates. In other words, the discussion on accretion product inhibition in Sect. 3.3 in the main text is largely speaking accurate: Peroxy radicals with α-NO$_2$ substituents, to the extent that they form, are not a source of accretion products.

The important caveat to this conclusion is that the DFT-level energetics might not be fully accurate. DLPNO-CCSD(T)-F12 single-point corrections for the electronic energy were attempted, but the ROHF reference wavefunction failed to converge for the transition states even after 1000 SCF cycles. The explanation for this is likely the high delocalisation of the spin density. In the Mulliken population analysis of the transition state structure, approximately $60 - 65$ % (depending on the system) of the spin density was located at the alkoxy oxygen and the rest distributed $10 - 15$ % each between the three atoms in the NO$_2$ leaving group. This leads us to suspect that the transition state has a highly multi-configuration character, meaning that post-DFT electronic energy corrections likely must be calculated using a multi-reference method. However, calculations like these are well beyond the scope of this work, as our main focus is in applying Structure-activity relationship results to in-complex RO reactions. The ωB97X-D3/jun-cc-pV(T+d)Z results are enough to conclude that the reaction likely occurs.
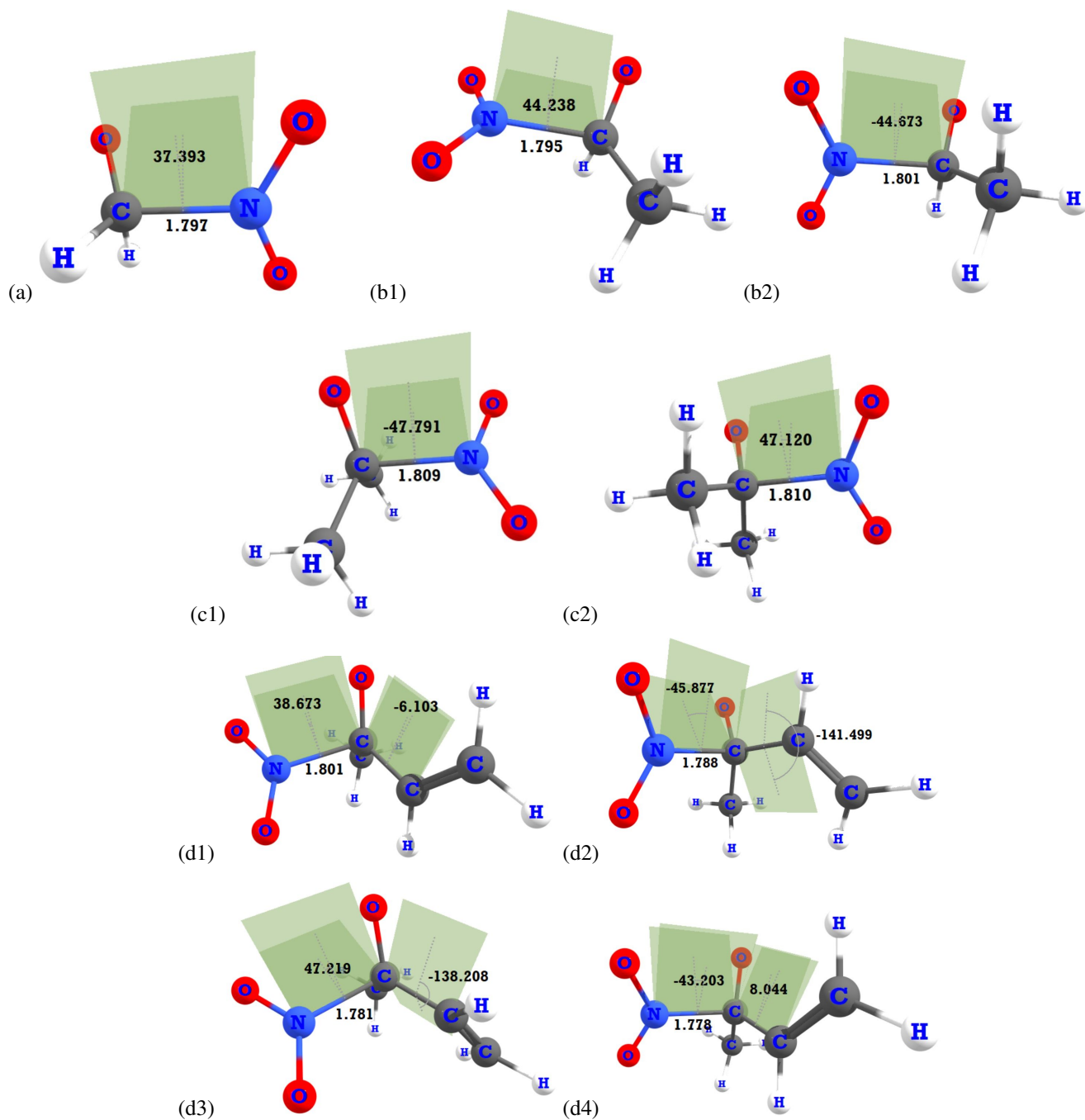
Figure S5. Molecular geometries of the transition states, with the most important geometric parameters, i.e. the CN bond length, the $\angle(CO\cdot, NO)$ dihedral angle, and the $\angle(CO\cdot, C=C)$ dihedral angle, shown.

(a) $CH_2(NO_2)O\cdot$ (b) $CH_3CH(NO_2)O\cdot$ TS 1 and 2 (c) $(CH_3)_2C(NO_2)O\cdot$ TS 1 and 2 (d) $CH_2=CHC(NO_2)O\cdot CH_3$ TS 1-4.

S4 Accuracy of Nannoolal Vapour Pressures

In a comparison study of different group contribution methods and computational methods for determining the saturation vapour pressures (p_{Sat}) of α-pinene derived oxidation products (Kurtén et al., 2016), unphysical values and odd trends were reported for the highly oxidized products in general and the (peroxide) accretion products in particular. Potential causes of these oddities were investigated by reproducing the molecules from that study in the Gecko structural format and comparing the article's reported p_{Sat}-values with those determined using GECKO-A's internal SIMPOL (Pankow and Asher, 2008) and Nannoolal (Nannoolal et al., 2004, 2008; Compernolle et al., 2010) p_{Sat} calculators, which have already proven themselves against experimental aerosol growth rates. (Barley and McFiggans, 2010; Valorso et al., 2011) The results are presented in Table S5. These results show that GECKO-A's native implementation produces different results from that of UManSysProp, (Topping) which was used by Kurtén et al. (2016), especially for the three C_{20} accretion products. In addition, the results are generally more in line with the other group contribution models. This suggests that the reported unphysical trends are due to UManSysProp's implementation of the Nannoolal model, not due to the model itself.

Name	n_{OOH}	COSMO[a]	Nan.[a]	EVAP.[a]	SIM.[a]	Nan.[b]	SIM.[b]
$C_{10}H_{16}O_4$-iso1	1	-6.0	-5.7	-6.0	-7.1	-7.0	-7.1
$C_{10}H_{16}O_4$-iso2	1	-7.3	-5.5	-5.8	-7.1	-6.7	-7.1
$C_{10}H_{16}O_4$-iso3	1	-6.7	-6.1	-6.1	-7.1	-6.8	-7.1
$C_{10}H_{16}O_5$	1	-6.0	-7.2	-7.7	-8.0	-8.4	-8.0
$C_{10}H_{16}O_6$-iso1	1	-5.5	-8.0	-8.0	-8.9	-9.1	-8.9
$C_{10}H_{16}O_6$-iso2	1	-8.1	-10.1	-10.5	-10.2	-11.4	-10.2
$C_{10}H_{16}O_7$-iso1	2	-5.9	-9.4	-9.5	-9.1	-10.7	-9.1
$C_{10}H_{16}O_7$-iso2	1	-8.8	-13.6	-12.0	-12.4	-13.9	-12.4
$C_{10}H_{16}O_8$-iso1	2	-8.0	-15.3	-13.7	-12.7	-15.7	-12.7
$C_{10}H_{16}O_8$-iso2	2	-6.4	-12.7	-11.0	-11.3	-13.0	-11.3
$C_{10}H_{16}O_8$-iso3	2	-8.1	-8.7	-9.2	-8.6	-9.6	-8.6
$C_{10}H_{16}O_9$	3	-6.6	-14.4	-12.7	-11.6	-14.7	-11.6
$C_{10}H_{16}O_{10}$	3	-7.5	-13.4	-12.7	-11.1	-13.4	-11.1
$C_{20}H_{30}O_{10}$-iso1	0	-11.9	-9.1	-13.7	-17.0	-17.4	-17.1
$C_{20}H_{30}O_{10}$-iso2	1	-12.2	-10.6	-14.9	-15.1	-16.7	-16.0
$C_{20}H_{30}O_{12}$	2	-10.1	-11.6	-16.7	-17.5	-20.7	-17.6

Table S5. $\log_{10}(p_{Sat}\,(\text{atm}))$ values predicted using different vapour pressure models. Nan: Nannoolal, SIM: SIMPOL, EVAP: EVAPORATION (Compernolle et al., 2011)

[a] Value from Kurtén et al. (2016). COSMO refers here specifically to the single conformer BP/TZVPD-FINE results, the most accurate computation performed for all 16 molecules.

[b] This work, using GECKO-A's vapour pressure calculators. (Valorso et al., 2011)

S5 Sensitivity Analysis of the Yield filter

To analyse the sensitivity of the $RO_2 + RO_2$ recombination yield cutoff, a simplified version of the GECKO-AP code was made that only calculated $y_{RO_2RO_2}$ for the list of RO_2's without generating product pathways. As a model precursor molecule for the sensitivity analysis, α-pinene was chosen due to being included in two of the three datasets, and due to having a suitably representative diversity of oxidation pathways. The RO_2's were generated up to the 5th generation with very low cutoff. ($y_c = 0.0005$) This resulted in a list of 32 199 RO_2's and 644 325 RO_2 pairs. Each radical was assigned a generation using the same method described in Sect. 2.2.2 of the main text, and the pairs were categorized based on the generation combination of the two radicals. Figure S6 shows the number of $RO_2 + RO_2$ pairs per generation where $y_{RO_2RO_2}$ lies above a certain yield cutoff. As seen in Figure S6 (b), higher generation pairings dominate the statistics at low yield cutoffs but are filtered out at higher ones. The latter is somewhat more desirable as we know that the theoretical maximum yields we are using to filter products are closer to reality in the initial generations. Based on the same graph, the range around 0.004-0.01 is where the recombination products of 3rd and 4th generation RO_2's with 2nd and 1st generation radicals start outnumbering the reactions where both radials are from the 3rd or 4th generation. This was thus treated as a good cutoff range for the DTA dataset where products were generated up to the 4th generation. For the Terpene dataset, managing the large amount of overall products was considered a more important criteria for the cutoff. Here 0.0025-0.004 was deemed a good cutoff range as here around 15-25 % of the 23 442 1st and 2nd generation RO_2 pairs remained. For the single generation β-caryophyllene dataset the cutoff 0.001 was deemed suitable, as this included the majority (251/404) of the 1st generation RO_2 pairs in this test run while still filtering out the least likely ones.

The removal of reaction pathways requiring simultaneously high concentrations of OH and NO_3 described in Sect. 2.2.2 of the main text was not performed here, as the necessary data curation is more involved. However, it is clear that this filtering criteria disproportional removed higher generation $RO_2 + RO_2$ pairs, as every generation by definition adds one more VOC + Oxidant step to the total mechanism. As such, this additional filtering step can be seen as yet another way to remove higher generation products whose importance is overestimated due to the usage of the theoretical maximum yields as $RO_2 + RO_2$ filtering criteria.
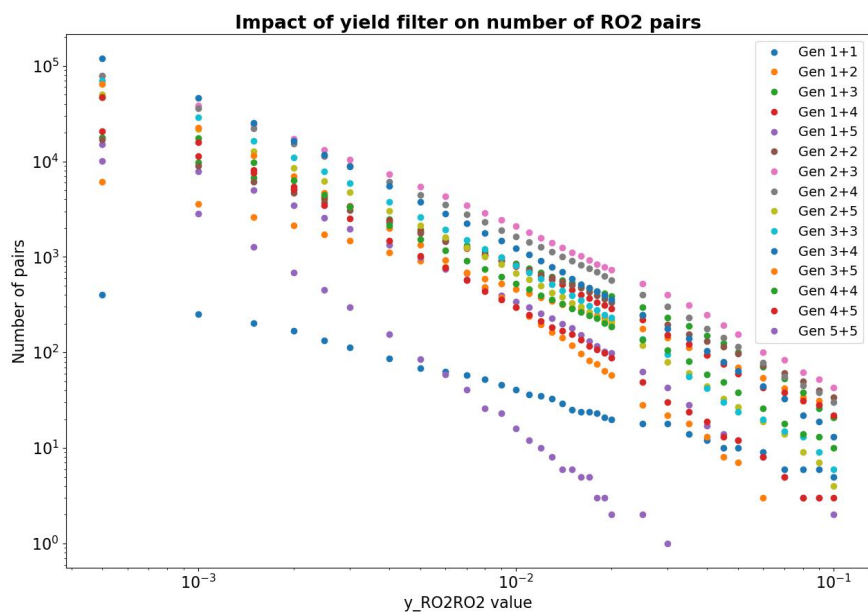
(a)
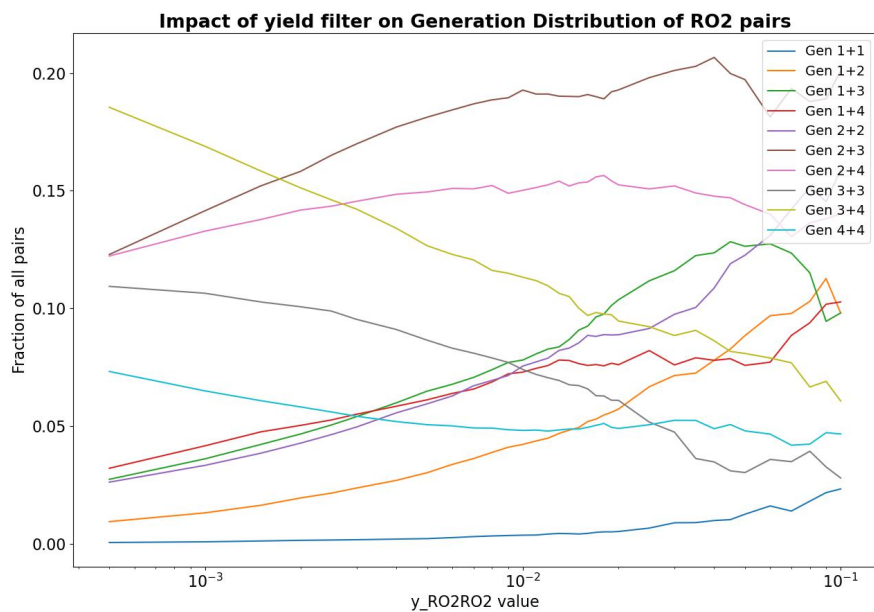
(b)

Figure S6. (a) The number of RO_2 pairs by generation as a function of $y_{RO_2RO_2}$ cutoff. As seen in the graph, higher generation products are filtered more heavily due to generally having lower theoretical maximum yields. (b) The number of RO_2 pairs by generation as a fraction of total number of RO_2 pairs. The 5th generation products are not shown to avoid clutter.

S6.1   DTA Dataset
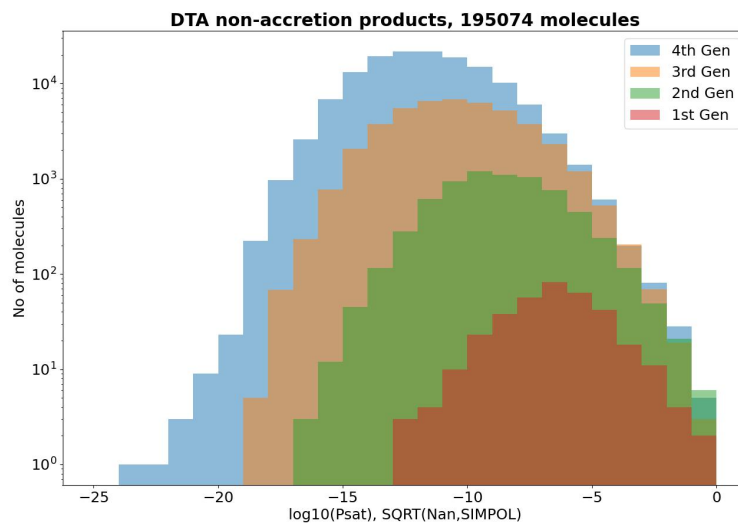
Figure S7. Saturation vapour pressure distribution of non-accretion products in the DTA Dataset.
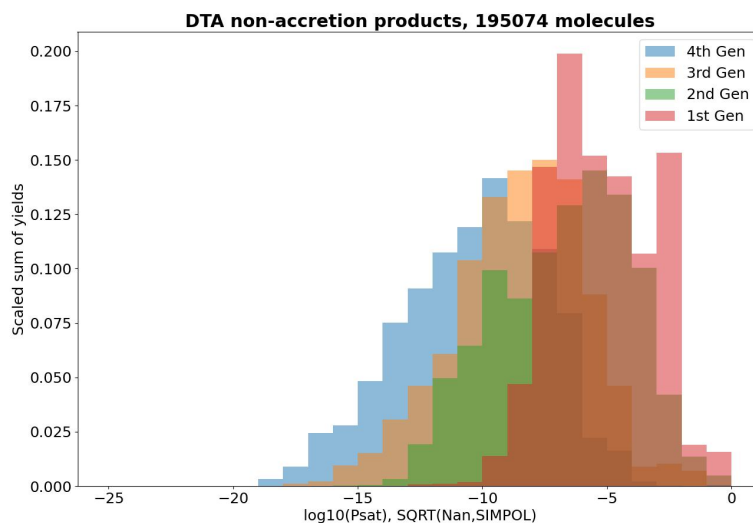
Figure S8. Saturation vapour pressure distribution of non-accretion products in the DTA Dataset, weighted by theoretical maximum yield and scaled down to ensure that $\sum y = 1$ for each generation.
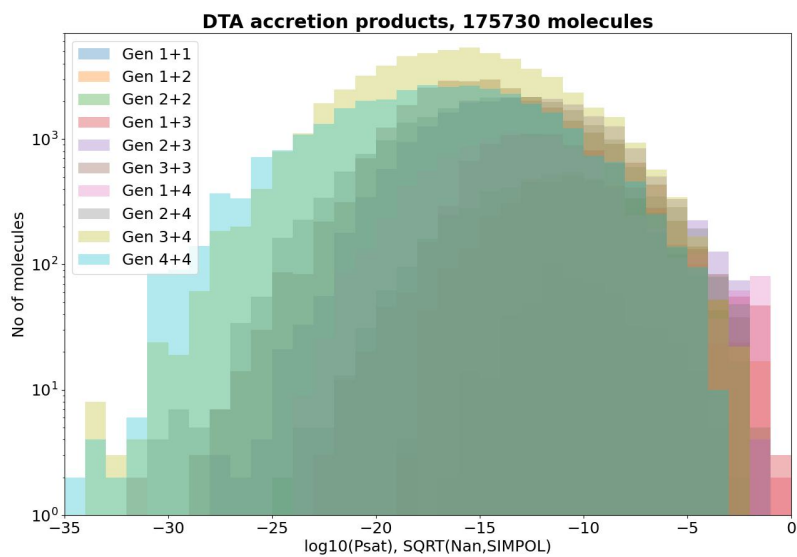
Figure S9. Saturation vapour pressure distribution of accretion products in the DTA Dataset.
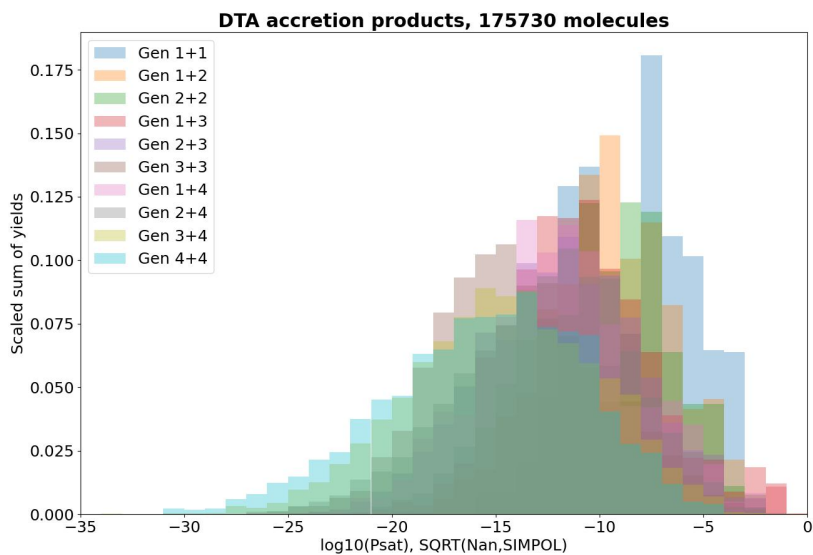
Figure S10. Saturation vapour pressure distribution of accretion products in the DTA Dataset, weighted by final yield y_{Prod} (Equation 10 in the main article) and scaled to ensure that $\sum y_{\mathrm{Prod}} = 1$ for each Gen n+m pair.

S6.2 Terpene Dataset
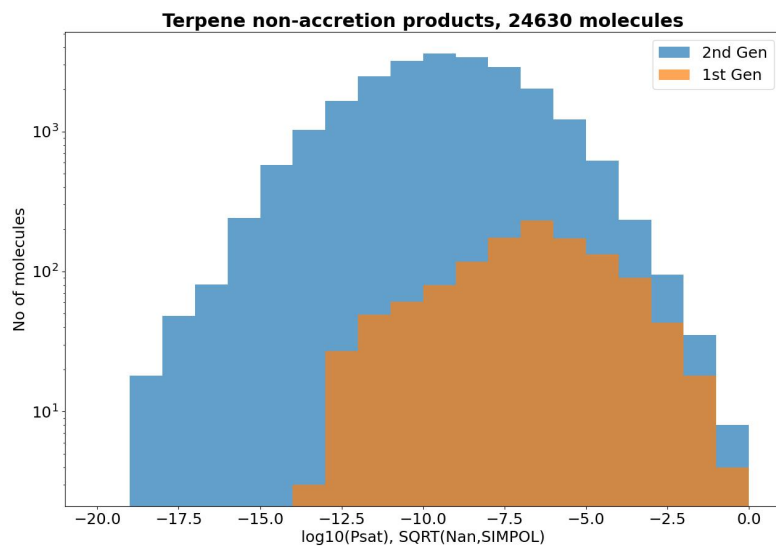
Figure S11. Saturation vapour pressure distribution of non-accretion products in the Terpene Dataset.
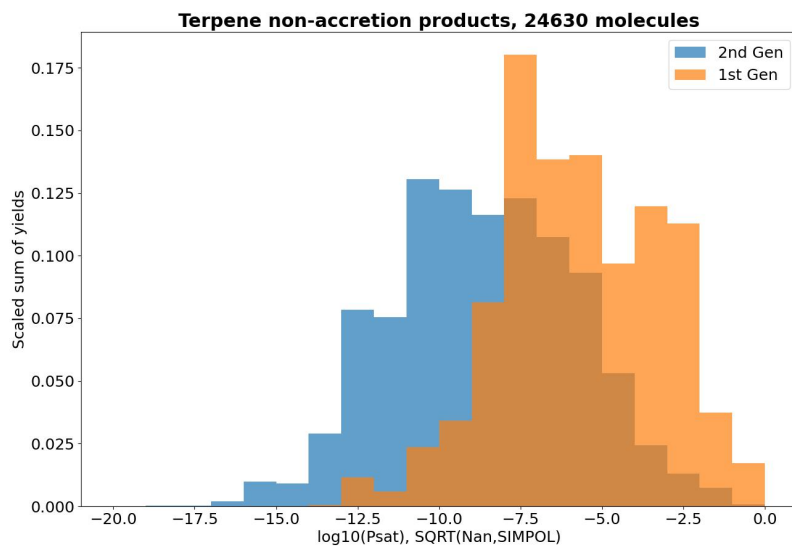
Figure S12. Saturation vapour pressure distribution of non-accretion products in the Terpene Dataset, weighted by theoretical maximum yield and scaled down to ensure that $\sum y = 1$ for each generation.
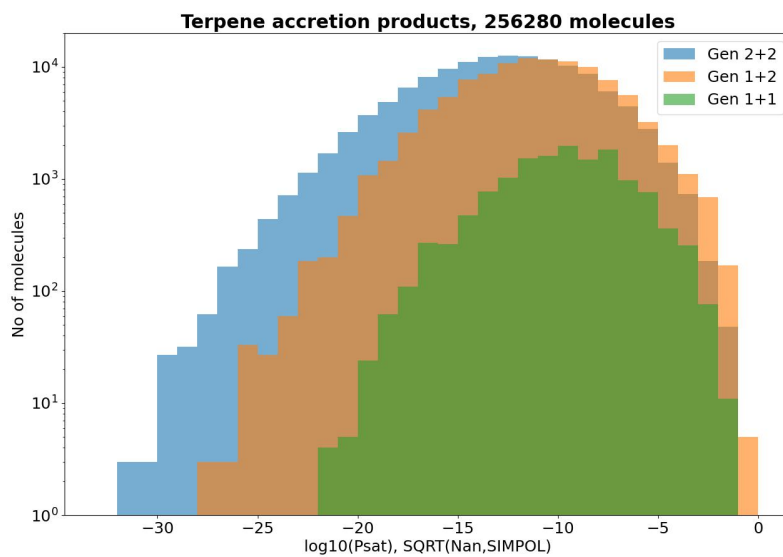
Figure S13. Saturation vapour pressure distribution of accretion products in the Terpene Dataset.
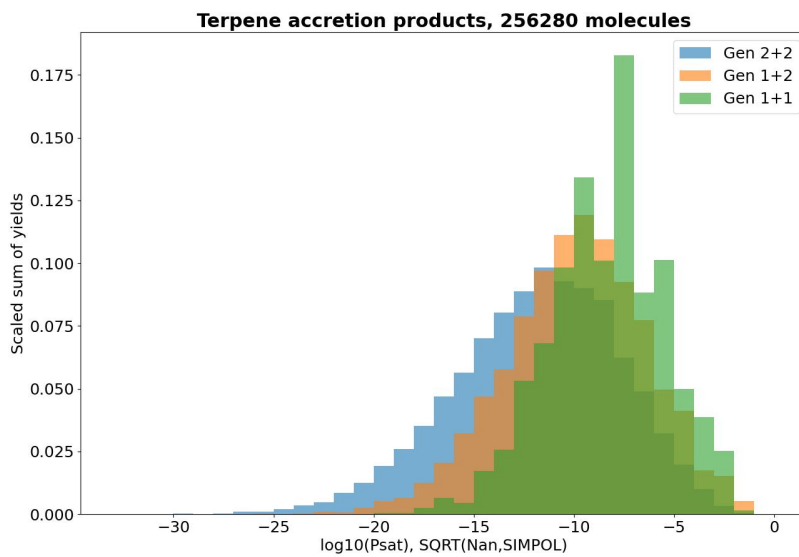
Figure S14. Saturation vapour pressure distribution of accretion products in the Terpene Dataset, weighted by final yield y_{Prod} (Equation 10 in the main article) and scaled to ensure that $\sum y_{\mathrm{Prod}} = 1$ for each Gen n+m pair.

S6.3 β-caryophyllene Dataset
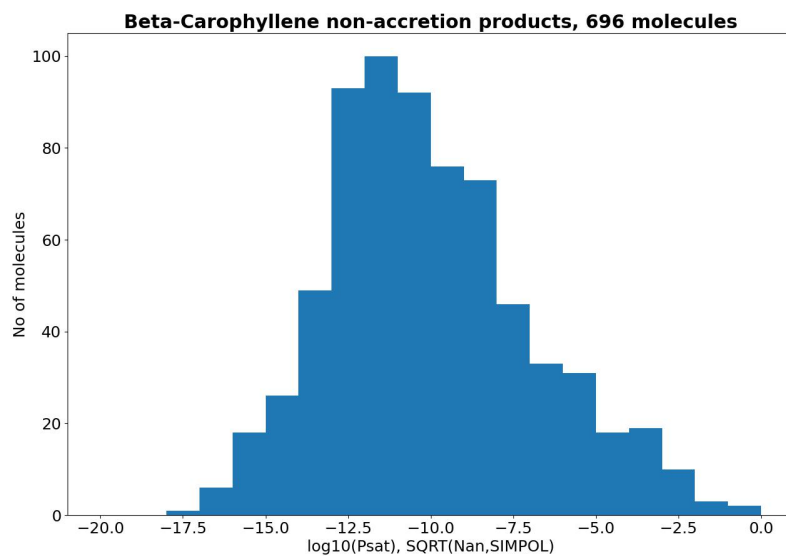
Figure S15. Saturation vapour pressure distribution of β-caryophyllene non-accretion products.
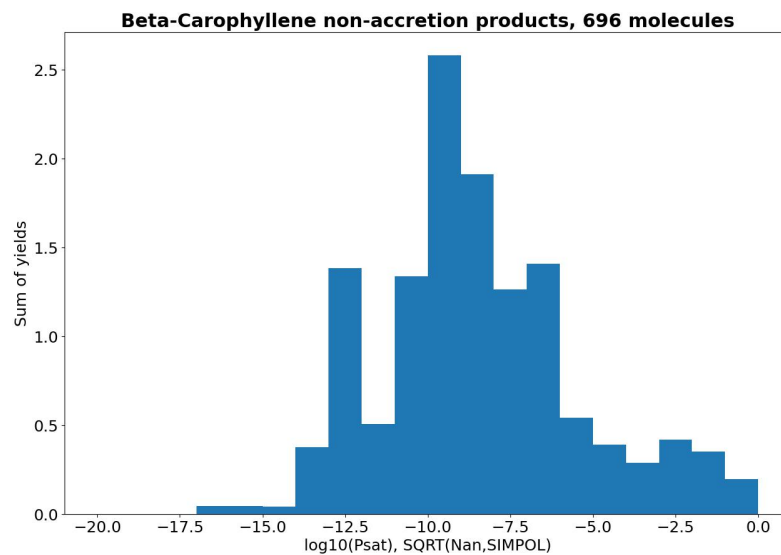
Figure S16. Saturation vapour pressure distribution of β-caryophyllene non-accretion products, weighted by theoretical maximum yield.
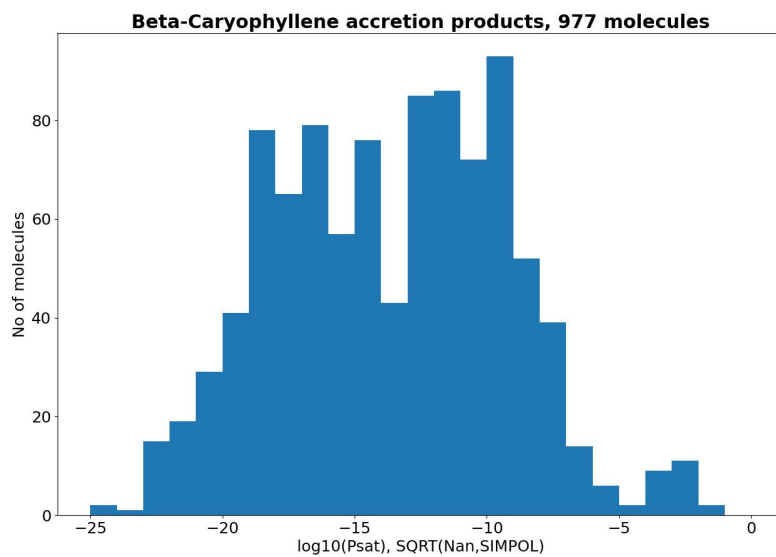
Figure S17. Saturation vapour pressure distribution of β-caryophyllene accretion products.
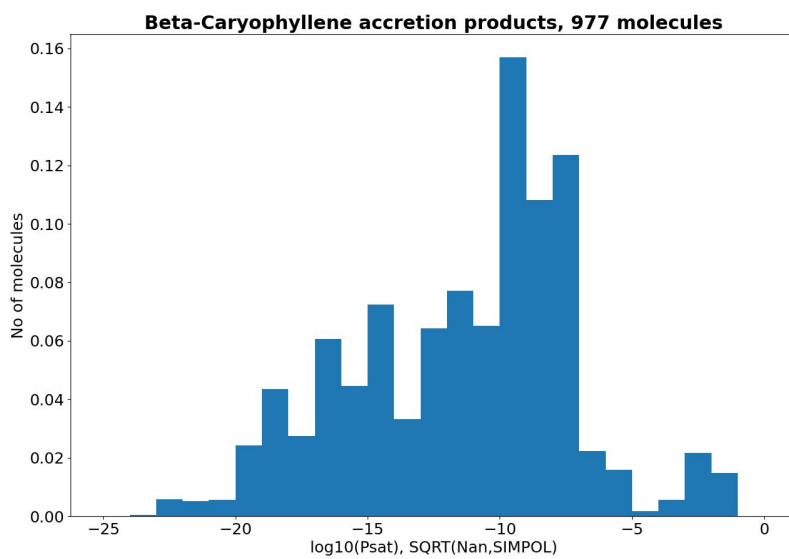
Figure S18. Saturation vapour pressure distribution of β-caryophyllene accretion products, weighted by final yield y_{Prod} (Equation 10 in the main article).
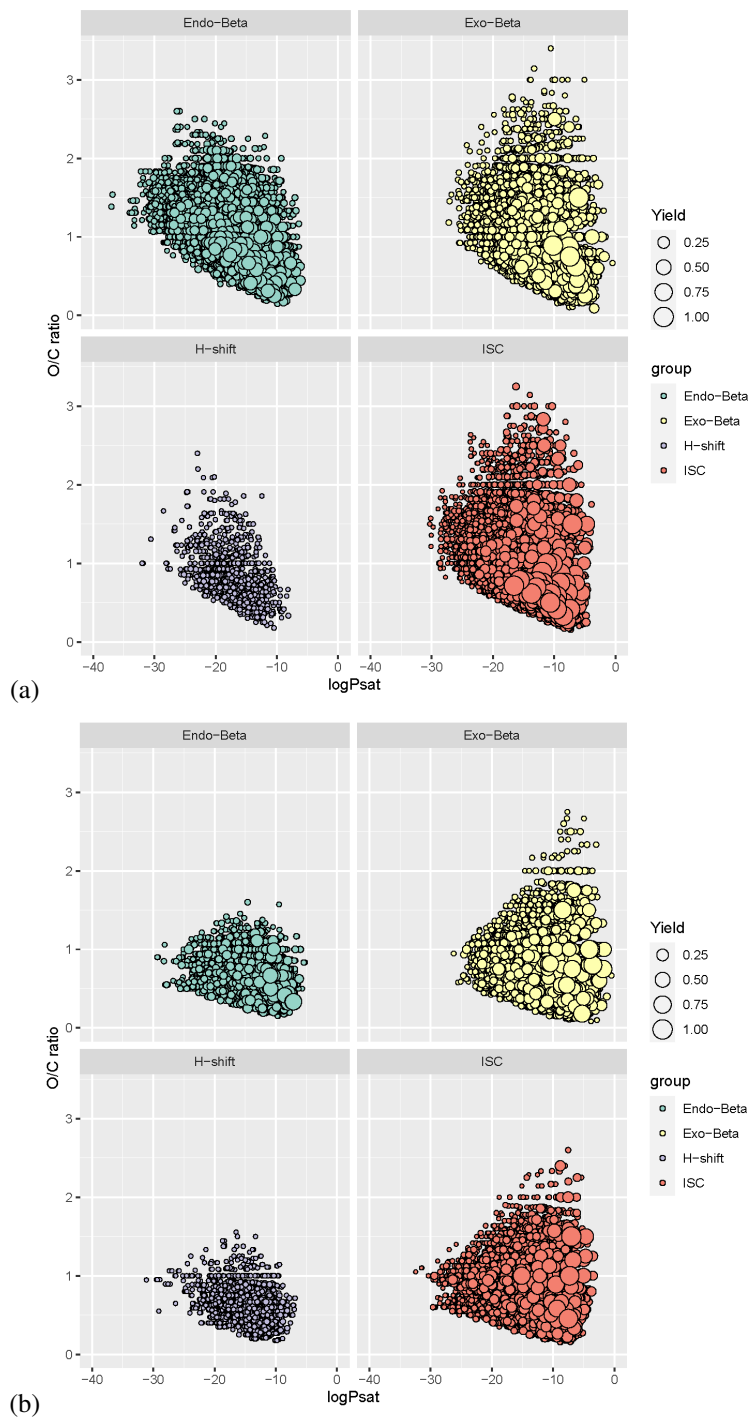
Figure S19. A bubble plot of the p_{Sat}-distribution of all accretion products categorized by reaction channel for (a) the DTA dataset and (b) for the Terpene dataset. p_{Sat} is expressed in atm.

S7 Tables on distributions of accretion product properties

In Sect. 3.4 of the main text we discussed our main observations from the data when analysing which $RO_2 + RO_2$ reaction channels lead to low-volatility products. In this section, the same topic is analysed more systematically with generation-by-generation tables on the numbers, yields, and ELVOC ($p_{Sat} < 10^{-13}$ atm) percentages.

S7.1 Distribution by Reaction Channel

The distribution of accretion products by in-complex reaction channel is presented for the Terpene dataset in Table S6, for the β-caryophyllene dataset (together with the distribution by VOC oxidant, explained properly in Sect. S7.3) in Table S7, and for the DTA dataset in Table S8.

Molecules	ISC	Exo-β	Endo-β	H-Shift	All
Gen 1+1	5 958	5 602	1 989	313	13 862
Gen 1+2	51 731	43 784	11 193	1 260	107 968
Gen 2+2	71 896	51 899	9 612	1 043	134 450
$\langle y_{\mathrm{Prod}} \rangle$	ISC	Exo-β	Endo-β	H-Shift	All
Gen 1+1	1.042 %	1.437 %	1.436 %	0.078 %	1.236 %
Gen 1+2	0.567 %	0.916 %	0.813 %	0.066 %	0.728 %
Gen 2+2	0.385 %	0.678 %	0.609 %	0.060 %	0.511 %
$p_{\mathrm{Sat}} < 10^{-13}$	ISC	Exo-β	Endo-β	H-Shift	All
Gen 1+1	18.0 %	2.8 %	32.8 %	33.9 %	14.3 %
Gen 1+2	40.2 %	10.2 %	53.9 %	57.9 %	29.7 %
Gen 2+2	62.2 %	23.0 %	62.5 %	73.0 %	47.2 %

Table S6. The amounts, average yields, and p_{Sat} distributions of the accretion products by reaction channel for the Terpene dataset.

Channel	ISC	Exo-β	Endo-β	H-Shift
Molecules	468	378	102	29
$\langle y_{\mathrm{Prod}} \rangle$	0.241 %	0.463 %	0.606 %	0.014 %
$p_{\mathrm{Sat}} < 10^{-13}$	66.0 %	27.0 %	68.6 %	86.2 %
Oxidant	OH	O_3	NO_3	All
Molecules	54	461	12	977
$\langle y_{\mathrm{Prod}} \rangle$	0.193 %	0.392 %	0.169 %	0.358 %
$p_{\mathrm{Sat}} < 10^{-13}$	68.5 %	46.2 %	41.7 %	51.8 %

Table S7. The amounts, average yields, and p_{Sat} distributions of the accretion products by reaction channel and oxidant for the β-caryophyllene dataset.

Molecules	ISC	Exo-β	Endo-β	H-Shift	All
Gen 1+1	213	45	254	22	534
Gen 1+2	1 647	987	1 329	93	4 056
Gen 2+2	2 260	1 615	934	61	4 870
Gen 1+3	3 445	1 595	3 738	123	8 901
Gen 2+3	9 446	5 933	6 511	207	22 097
Gen 3+3	10 599	5 709	10 898	194	27 400
Gen 1+4	4 018	2 020	4 008	140	10 186
Gen 2+4	10 818	6 794	5 869	215	23 696
Gen 3+4	23 100	13 345	21 144	402	57 991
Gen 4+4	14 287	9 043	9 713	103	33 146
$\langle y_{\mathrm{Prod}} \rangle$	ISC	Exo-β	Endo-β	H-Shift	All
Gen 1+1	0.812 %	3.492 %	1.714 %	0.152 %	1.439 %
Gen 1+2	0.607 %	1.133 %	1.116 %	0.092 %	0.890 %
Gen 2+2	0.699 %	1.122 %	0.833 %	0.088 %	0.857 %
Gen 1+3	0.472 %	1.147 %	1.197 %	0.100 %	0.892 %
Gen 2+3	0.509 %	0.934 %	0.944 %	0.107 %	0.748 %
Gen 3+3	0.330 %	0.776 %	0.869 %	0.104 %	0.636 %
Gen 1+4	0.663 %	1.281 %	1.151 %	0.135 %	0.970 %
Gen 2+4	0.785 %	1.207 %	1.025 %	0.101 %	0.959 %
Gen 3+4	0.568 %	1.061 %	0.957 %	0.128 %	0.820 %
Gen 4+4	0.829 %	1.194 %	1.076 %	0.103 %	0.999 %
$p_{\mathrm{Sat}} < 10^{-13}$	ISC	Exo-β	Endo-β	H-Shift	All
Gen 1+1	10.8 %	2.2 %	14.2 %	54.5 %	13.5 %
Gen 1+2	15.5 %	4.2 %	36.8 %	43.0 %	20.3 %
Gen 2+2	35.2 %	20.6 %	56.5 %	52.5 %	34.7 %
Gen 1+3	27.1 %	4.5 %	57.9 %	64.2 %	36.5 %
Gen 2+3	49.2 %	22.0 %	78.1 %	87.9 %	50.8 %
Gen 3+3	65.2 %	27.1 %	89.9 %	96.4 %	67.3 %
Gen 1+4	45.7 %	9.3 %	77.7 %	89.3 %	51.7 %
Gen 2+4	60.6 %	29.7 %	89.0 %	94.9 %	59.1 %
Gen 3+4	77.1 %	37.3 %	96.0 %	99.5 %	75.0 %
Gen 4+4	86.1 %	45.8 %	97.8 %	100 %	78.6 %

Table S8. The amounts, average yields, and p_{Sat} distributions of the accretion products by in-complex reaction channel for the DTA dataset.

Here we largely see the same trends already discussed in the main article. Endocyclic β-scission products have generally the lowest volatilities, apart from H-shift products, which have even lower volatilities but also low yields.

S7.2 Distribution by Precursor Molecule

160 The accretion products are categorized by precursor molecule in Table S10 for the DTA dataset and in Table S11 for the Terpene dataset. As the RO_2 are not limited to only reacting with RO_2 formed from other precursor molecules (in the code or in reality), we group the products both exclusively (e.g. both RO_2 must be derived from Isoprene) and inclusively (e.g. Either RO_2 can be derived from Isoprene).

Molecules	B. Iso	B. α-pin	B. β-pin	B. Lim	B. β-oci	B. Sabi	B. Δ-Car	B. Myr
Gen 1+1	414	420	618	1 988	492	465	190	968
Gen 1+2	1 749	3 875	5 568	16 814	4 013	3 134	2 121	7 903
Gen 2+2	1 111	4 760	5 380	14 594	3 707	2 208	2 820	7 444
$\langle y_{\mathrm{Prod}} \rangle$	B. Iso	B. α-pin	B. β-pin	B. Lim	B. β-oci	B. Sabi	B. Δ-Car	B. Myr
Gen 1+1	3.636 %	3.093 %	3.533 %	1.789 %	3.117 %	3.311 %	4.216 %	2.533 %
Gen 1+2	1.633 %	1.289 %	1.143 %	0.859 %	1.370 %	0.971 %	1.392 %	1.175 %
Gen 2+2	0.737 %	0.658 %	0.577 %	0.497 %	0.680 %	0.441 %	0.660 %	0.690 %
$p_{\mathrm{Sat}} < 10^{-13}$	B. Iso	B. α-pin	B. β-pin	B. Lim	B. β-oci	B. Sabi	B. Δ-Car	B. Myr
Gen 1+1	1.0 %	7.9 %	21.4 %	3.8 %	1.4 %	21.5 %	0.0 %	6.5 %
Gen 1+2	5.8 %	15.0 %	30.6 %	20.6 %	9.8 %	24.5 %	10.0 %	19.3 %
Gen 2+2	15.3 %	33.7 %	48.5 %	34.5 %	22.7 %	37.8 %	22.1 %	37.3 %
Molecules	E. Iso	E. α-pin	E. β-pin	E. Lim	E. β-oci	E. Sabi	E. Δ-Car	E. Myr
Gen 1+1	4 864	4 183	5 265	9 130	5 189	4 255	3 641	6 539
Gen 1+2	37 660	38 704	44 901	70 370	42 739	35 532	34 267	53 399
Gen 2+2	26 856	49 240	50 115	72 661	43 203	32 829	40 175	57 831
$\langle y_{\mathrm{Prod}} \rangle$	E. Iso	E. α-pin	E. β-pin	E. Lim	E. β-oci	E. Sabi	E. Δ-Car	E. Myr
Gen 1+1	2.131 %	2.187 %	1.914 %	1.474 %	1.977 %	2.103 %	2.356 %	1.741 %
Gen 1+2	1.065 %	1.039 %	0.950 %	0.801 %	0.992 %	1.004 %	1.075 %	0.906 %
Gen 2+2	0.619 %	0.568 %	0.537 %	0.511 %	0.581 %	0.516 %	0.569 %	0.577 %
$p_{\mathrm{Sat}} < 10^{-13}$	E. Iso	E. α-pin	E. β-pin	E. Lim	E. β-oci	E. Sabi	E. Δ-Car	E. Myr
Gen 1+1	6.8 %	11.9 %	17.8 %	10.0 %	7.0 %	17.7 %	7.4 %	10.4 %
Gen 1+2	16.8 %	22.1 %	28.7 %	25.1 %	19.0 %	24.1 %	18.5 %	23.0 %
Gen 2+2	30.3 %	41.3 %	47.5 %	41.5 %	34.1 %	40.1 %	35.1 %	41.3 %

Table S9. The amounts, average yields, and p_{Sat} distributions of the accretion products by peroxy radical precursor molecules. 'B.' and 'E.' are short for 'Both' and 'Either', respectively.

Molecules	B. Dec	B. Tol	B. α-pin	E. Dec	E. Tol	E. α-pin
Gen 1+1	25	124	93	222	457	367
Gen 1+2	430	974	1 110	1 868	3 369	3 212
Gen 2+2	169	1 061	2 368	1 484	3 494	4 431
Gen 1+3	248	2 695	2 054	3 110	7 937	6 419
Gen 2+3	335	6 658	7 270	5 816	18 205	17 629
Gen 3+3	259	10 436	4 766	5 436	24 812	19 074
Gen 1+4	110	4 585	1 623	3 167	9 713	6 367
Gen 2+4	47	9 159	4 609	4 860	21 698	17 421
Gen 3+4	51	28 520	5 011	6 729	55 923	33 387
Gen 4+4	0	19 785	1 525	1 412	32 890	14 607
$\langle y_{\mathrm{Prod}} \rangle$	B. Dec	B. Tol	B. α-pin	E. Dec	E. Tol	E. α-pin
Gen 1+1	5.948 %	1.775 %	1.858 %	2.170 %	1.513 %	1.752 %
Gen 1+2	0.650 %	1.046 %	1.240 %	0.899 %	0.919 %	0.976 %
Gen 2+2	0.465 %	1.100 %	1.043 %	0.822 %	0.937 %	0.889 %
Gen 1+3	0.664 %	1.232 %	0.977 %	1.034 %	0.923 %	0.895 %
Gen 2+3	0.505 %	0.943 %	0.761 %	0.734 %	0.799 %	0.785 %
Gen 3+3	0.598 %	0.819 %	0.505 %	0.668 %	0.663 %	0.585 %
Gen 1+4	0.342 %	1.152 %	0.744 %	1.064 %	0.989 %	1.001 %
Gen 2+4	0.311 %	1.151 %	0.790 %	0.866 %	1.006 %	1.024 %
Gen 3+4	0.397 %	0.986 %	0.627 %	0.828 %	0.839 %	0.762 %
Gen 4+4	-	1.221 %	0.809 %	0.523 %	1.004 %	0.855 %
$p_{\mathrm{Sat}} < 10^{-13}$	B. Dec	B. Tol	B. α-pin	E. Dec	E. Tol	E. α-pin
Gen 1+1	0.0 %	18.5 %	8.6 %	5.9 %	13.1 %	11.4 %
Gen 1+2	0.0 %	20.8 %	17.0 %	6.3 %	18.0 %	18.0 %
Gen 2+2	0.0 %	28.2 %	33.2 %	11.9 %	26.6 %	33.6 %
Gen 1+3	0.0 %	36.3 %	19.6 %	15.2 %	36.5 %	31.4 %
Gen 2+3	1.5 %	50.0 %	37.3 %	25.2 %	50.0 %	46.5 %
Gen 3+3	3.1 %	75.1 %	43.1 %	28.8 %	69.1 %	62.9 %
Gen 1+4	0.0 %	54.4 %	23.8 %	24.9 %	51.3 %	43.0 %
Gen 2+4	0.0 %	59.9 %	45.4 %	33.9 %	58.2 %	56.1 %
Gen 3+4	5.9 %	81.9 %	51.7 %	44.3 %	75.3 %	68.9 %
Gen 4+4	0.0 %	84.3 %	48.8 %	38.7 %	78.5 %	71.8 %

Table S10. The amounts, average yields, and p_{Sat} distributions distributions of the accretion products by peroxy radical precursor molecules.
'B.' and 'E.' are short for 'Both' and 'Either', respectively.

The main trend observed when categorizing the accretion products by precursor molecule were already discussed in the main article.

S7.3 Distribution by VOC Oxidant

The accretion products are categorized by required oxidants in Table S12. This is a somewhat fuzzy categorization, as higher generation radicals need multiple VOC + Oxidant steps to form, and as the two RO_2 forming the reactive pair have different formation pathways. Due to this complexity the following tables were made with a simple but consistent criteria: Accretion product where both reactant RO_2 have OH oxidation at some point in their formation mechanism are classified as OH-derived. The results are presented for the Terpene dataset in Table S11 and for the DTA dataset in Table S12.

Molecules	OH	O_3	NO_3	All
Gen 1+1	6 280	2 569	2 735	13 862
Gen 1+2	51 488	23 710	31 012	107 968
Gen 2+2	60 490	24 578	58 201	134 450
$\langle y_{\mathrm{Prod}} \rangle$	OH	O_3	NO_3	All
Gen 1+1	1.367 %	1.364 %	1.754 %	1.236 %
Gen 1+2	0.684 %	0.710 %	0.982 %	0.728 %
Gen 2+2	0.442 %	0.444 %	0.594 %	0.511 %
$p_{\mathrm{Sat}} < 10^{-13}$	OH	O_3	NO_3	All
Gen 1+1	11.7 %	4.6 %	22.0 %	14.3 %
Gen 1+2	23.6 %	16.7 %	36.1 %	29.7 %
Gen 2+2	37.1 %	31.7 %	57.1 %	47.2 %

Table S11. The amounts, average yields, and p_{Sat} distributions of the accretion products by VOC oxidant in the Terpene dataset.

These results from these tables are largely unsurprising: OH oxidation produces both the most diverse set of accretion products, due to producing the most diverse set of radicals, and generally also the lowest vapour pressures, due to OH addition being a more common reaction channel than NO_3 addition.

Molecules	OH	O_3	NO_3	All
Gen 1+1	326	15	18	534
Gen 1+2	3 211	290	490	4 056
Gen 2+2	4 025	986	1 573	4 870
Gen 1+3	7 208	392	495	8 901
Gen 2+3	20 224	2 922	4 171	22 097
Gen 3+3	26 482	1 489	2 247	27 400
Gen 1+4	8 508	419	455	10 186
Gen 2+4	21 965	3 359	3 775	23 696
Gen 3+4	55 899	2 882	4 880	57 991
Gen 4+4	31 924	1 500	2 950	33 146
$\langle y_{\mathrm{Prod}} \rangle$	OH	O_3	NO_3	All
Gen 1+1	1.820 %	1.461 %	0.822 %	1.439 %
Gen 1+2	0.908 %	1.160 %	0.788 %	0.890 %
Gen 2+2	0.901 %	1.299 %	0.791 %	0.857 %
Gen 1+3	0.925 %	0.732 %	0.741 %	0.892 %
Gen 2+3	0.765 %	0.813 %	0.647 %	0.748 %
Gen 3+3	0.640 %	0.509 %	0.621 %	0.636 %
Gen 1+4	0.959 %	0.839 %	1.066 %	0.970 %
Gen 2+4	0.969 %	0.890 %	1.018 %	0.959 %
Gen 3+4	0.821 %	0.698 %	1.035 %	0.820 %
Gen 4+4	1.004 %	0.847 %	1.131 %	0.999 %
$p_{\mathrm{Sat}} < 10^{-13}$	OH	O_3	NO_3	All
Gen 1+1	13.8 %	0.0 %	0.0 %	13.5 %
Gen 1+2	18.4 %	23.4 %	15.9 %	20.3 %
Gen 2+2	31.9 %	36.5 %	38.3 %	34.7 %
Gen 1+3	33.4 %	37.2 %	17.6 %	36.5 %
Gen 2+3	50.8 %	45.7 %	43.5 %	50.8 %
Gen 3+3	67.8 %	55.7 %	51.7 %	67.3 %
Gen 1+4	50.0 %	45.6 %	41.5 %	51.7 %
Gen 2+4	59.3 %	52.0 %	50.6 %	59.1 %
Gen 3+4	75.7 %	56.6 %	53.6 %	75.0 %
Gen 4+4	79.5 %	57.9 %	54.7 %	78.6 %

Table S12. The amounts, average yields, and vapour pressure distributions of the accretion products by VOC oxidant.

175 ## S7.4 Distribution by RO$_2$ class

Finally, the only variable in the data we haven't looked at is the RO$_2$ rate class. In the tables below, all the accretion products where one of the two RO$_2$ belongs to a specific rate class and generation are grouped together. MetC(O)O$_2$ is listed separately, as it is the only RC(O)O$_2$ for which we did not apply the smaller recombination yield factor due to an assumed autoxidation sink. This is presented in Table S13 for the DTA dataset and Table S14 for the Terpene and β-cayophyllene datasets.

Molecules	1	3	4	5	7	8	9	MetC(O)O$_2$
Gen 1	135	405	4 234	192	4 351	9 221	815	4 799
Gen 2	355	882	3 508	31	22 203	25 313	6 192	0
Gen 3	436	3 650	7 101	1 078	43 165	75 945	4 808	0
Gen 4	155	2 376	7 514	567	56 529	75 914	7 940	0
$\langle y_{\mathrm{Prod}} \rangle$	1	3	4	5	7	8	9	MetC(O)O$_2$
Gen 1	0.572 %	0.765 %	0.749 %	0.423 %	1.317 %	0.737 %	0.565 %	1.302 %
Gen 2	0.742 %	0.746 %	0.783 %	0.594 %	0.840 %	0.946 %	0.610 %	-
Gen 3	0.824 %	0.726 %	0.669 %	0.841 %	0.743 %	0.761 %	0.528 %	-
Gen 4	0.600 %	0.603 %	0.989 %	0.827 %	0.700 %	1.082 %	0.635 %	-
$p_{\mathrm{Sat}} < 10^{-13}$	1	3	4	5	7	8	9	MetC(O)O$_2$
Gen 1	20.0 %	43.5 %	39.7 %	27.1 %	44.8 %	51.1 %	56.3 %	8.4 %
Gen 2	20.6 %	43.3 %	33.1 %	54.8 %	54.7 %	54.2 %	26.0 %	-
Gen 3	39.4 %	36.5 %	68.4 %	83.5 %	57.7 %	72.6 %	42.8 %	-
Gen 4	19.4 %	45.5 %	58.3 %	97.7 %	76.0 %	73.3 %	53.3 %	-

Table S13. The amounts, average yields, and vapour pressure distributions of the accretion products by RO$_2$ rate class in the DTA dataset.

180 The main observation from these tables is a fully expected result: The list of RO$_2$ pairs is dominated by RO$_2$ at the faster end of the recombination rate scale. Acyl peroxy radicals (rate class 9) are not quite as dominant, but that is likely fully explained by the fact that we scaled down their recombination yields due to the assumed autoxidation sink. The results for MetC(O)O$_2$ are also interesting but expected: The number of RO$_2$ pairs including it is large, but they typically do not have low vapour pressures, presumably due to their lower-than-average size. These results underline that there are always two factors to which

185 RO$_2$ pairs contribute the most to ELVOC formation: recombination rates and low-volatility products with large branching ratios. MetC(O)O$_2$ + RO$_2$ pairs fill the first criteria, but often not the second.

Molecules	1	3	4	5	7	8	9	MetC(O)O$_2$
Gen 1	895	9 299	9 357	9 946	44 924	48 725	3 825	5 888
Gen 2	2 725	26 270	14 781	13 439	145 346	117 729	26 816	0
β-Car.	56	145	145	180	618	338	92	216
$\langle y_{\text{Prod}} \rangle$	1	3	4	5	7	8	9	MetC(O)O$_2$
Gen 1	0.770 %	0.595 %	0.586 %	0.638 %	0.726 %	0.892 %	0.456 %	2.366 %
Gen 2	0.724 %	0.518 %	0.587 %	0.653 %	0.609 %	0.594 %	0.384 %	-
β-Car.	0.453 %	0.564 %	0.193 %	0.229 %	0.308 %	0.343 %	0.135 %	0.751 %
$p_{\text{Sat}} < 10^{-13}$	1	3	4	5	7	8	9	MetC(O)O$_2$
Gen 1	29.2 %	32.1 %	43.9 %	23.0 %	27.6 %	26.2 %	18.1 %	3.7 %
Gen 2	36.1 %	45.7 %	39.5 %	45.6 %	41.3 %	44.8 %	30.3 %	-
β-Car.	19.6 %	62.8 %	55.9 %	57.2 %	58.9 %	52.1 %	71.7 %	6.5 %

Table S14. The amounts, average yields, and vapour pressure distributions of the accretion products by RO$_2$ rate class in the Terpene and β-caryophyllene datasets.

References

Barley, M. and McFiggans, G.: The critical assessment of vapour pressure estimation methods for use in modelling the formation of atmospheric organic aerosol, Atmospheric Chemistry and Physics, 10, 749–767, 2010.

190 Bianchi, F., Kurtén, T., Riva, M., Mohr, C., Rissanen, M. P., Roldin, P., Berndt, T., Crounse, J. D., Wennberg, P. O., Mentel, T. F., et al.: Highly oxygenated organic molecules (HOM) from gas-phase autoxidation involving peroxy radicals: A key contributor to atmospheric aerosol, Chemical reviews, 119, 3472–3509, 2019.

Compernolle, S., Ceulemans, K., and Müller, J.-F.: Vapor pressure estimation methods applied to secondary organic aerosol constituents from α-pinene oxidation: an intercomparison study, Atmospheric Chemistry and Physics, 10, 6271–6282, 2010.

195 Compernolle, S., Ceulemans, K., and Müller, J.-F.: EVAPORATION: a new vapour pressure estimation methodfor organic molecules including non-additivity and intramolecular interactions, Atmospheric Chemistry and Physics, 11, 9431–9450, 2011.

Eckart, C.: The penetration of a potential barrier by electrons, Physical Review, 35, 1303, 1930.

Franzon, L.: Simple Physical Model for the Estimation of Irreversible Dissociation Rates for Bimolecular Complexes, The Journal of Physical Chemistry A, 127, 5956–5966, 2023.

200 Grimme, S.: Supramolecular binding thermodynamics by dispersion-corrected density functional theory, Chemistry–A European Journal, 18, 9955–9964, 2012.

Hasan, G.: Computational Studies of Reaction Channels for ^{3}(RO...OR) Intermediates formed in Peroxy Self and Cross-Reactions, Ph.D. thesis, University of Helsinki, 2023.

Ishida, K., Morokuma, K., and Komornicki, A.: The intrinsic reaction coordinate. An ab initio calculation for HNC$\longrightarrow$ HCN and H$-$ $^+$CH$_4$,
205 The Journal of Chemical Physics, 66, 2153–2156, 1977.

Jenkin, M. E., Valorso, R., Aumont, B., and Rickard, A. R.: Estimation of rate coefficients and branching ratios for reactions of organic peroxy radicals for use in automated mechanism construction, Atmospheric Chemistry and Physics, 19, 7691–7717, 2019.

Johnston, H. S. and Heicklen, J.: Tunnelling corrections for unsymmetrical Eckart potential energy barriers, The Journal of Physical Chemistry, 66, 532–533, 1962.

210 Kurtén, T., Tiusanen, K., Roldin, P., Rissanen, M., Luy, J.-N., Boy, M., Ehn, M., and Donahue, N.: α-Pinene autoxidation products may not have extremely low saturation vapor pressures despite high O: C ratios, The Journal of Physical Chemistry A, 120, 2569–2582, 2016.

Lin, Y.-S., Li, G.-D., Mao, S.-P., and Chai, J.-D.: Long-range corrected hybrid density functionals with improved dispersion corrections, Journal of Chemical Theory and Computation, 9, 263–272, 2013.

Møller, K. H., Otkjær, R. V., Hyttinen, N., Kurtén, T., and Kjaergaard, H. G.: Cost-effective implementation of multiconformer transition
215 state theory for peroxy radical hydrogen shift reactions, The Journal of Physical Chemistry A, 120, 10 072–10 087, 2016.

Nannoolal, Y., Rarey, J., Ramjugernath, D., and Cordes, W.: Estimation of pure component properties: Part 1. Estimation of the normal boiling point of non-electrolyte organic compounds via group contributions and group interactions, Fluid Phase Equilibria, 226, 45–63, 2004.

Nannoolal, Y., Rarey, J., and Ramjugernath, D.: Estimation of pure component properties: Part 3. Estimation of the vapor pressure of non-
220 electrolyte organic compounds via group contributions and group interactions, Fluid Phase Equilibria, 269, 117–133, 2008.

Neese, F.: Software update: The ORCA program system - Version 5.0, WIREs Computational Molecular Science, 12, https://doi.org/10.1002/wcms.1606, 2022.

Pankow, J. F. and Asher, W. E.: SIMPOL. 1: a simple group contribution method for predicting vapor pressures and enthalpies of vaporization of multifunctional organic compounds, Atmospheric Chemistry and Physics, 8, 2773–2796, 2008.

225 Papajak, E., Zheng, J., Xu, X., Leverentz, H. R., and Truhlar, D. G.: Perspectives on basis sets beautiful: Seasonal plantings of diffuse basis functions, Journal of chemical theory and computation, 7, 3027–3034, 2011.

Peräkylä, O., Berndt, T., Franzon, L., Hasan, G., Meder, M., Valiev, R. R., Daub, C. D., Varelas, J. G., Geiger, F. M., Thomson, R. J., et al.: Large Gas-Phase Source of Esters and Other Accretion Products in the Atmosphere, Journal of the American Chemical Society, 145, 7780–7790, 2023.

230 Pracht, P., Bohle, F., and Grimme, S.: Automated exploration of the low-energy chemical space with fast quantum chemical methods, Physical Chemistry Chemical Physics, 22, 7169–7192, 2020.

Rissanen, M. P., Kurtén, T., Sipilä, M., Thornton, J. A., Kangasluoma, J., Sarnela, N., Junninen, H., Jørgensen, S., Schallhart, S., Kajos, M. K., et al.: The formation of highly oxidized multifunctional products in the ozonolysis of cyclohexene, Journal of the American Chemical Society, 136, 15 596–15 606, 2014.

235 Seal, P., Barua, S., Iyer, S., Kumar, A., and Rissanen, M.: A systematic study on the kinetics of H-shift reactions in pristine acyl peroxy radicals, Physical Chemistry Chemical Physics, 25, 28 205–28 212, 2023.

Stephens, P. J., Devlin, F. J., Chabalowski, C. F., and Frisch, M. J.: Ab initio calculation of vibrational absorption and circular dichroism spectra using density functional force fields, The Journal of physical chemistry, 98, 11 623–11 627, 1994.

Topping, D.: UManSysProp Multiphase system online property prediction, http://http://umansysprop.seaes.manchester.ac.uk.

240 Valorso, R., Aumont, B., Camredon, M., Raventos-Duran, T., Mouchel-Vallon, C., Ng, N., Seinfeld, J. H., Lee-Taylor, J., and Madronich, S.: Explicit modelling of SOA formation from α-pinene photooxidation: sensitivity to vapour pressure estimation, Atmospheric Chemistry and Physics, 11, 6895–6910, 2011.

Vereecken, L. and Nozière, B.: H migration in peroxy radicals under atmospheric conditions, Atmospheric chemistry and physics, 20, 7429–7458, 2020.

245 Vereecken, L. and Peeters, J.: Decomposition of substituted alkoxy radicals—part I: a generalized structure–activity relationship for reaction barrier heights, Physical Chemistry Chemical Physics, 11, 9062–9074, 2009.

Villenave, E., Lesclaux, R., Seefeld, S., and Stockwell, W. R.: Kinetics and atmospheric implications of peroxy radical cross reactions involving the $CH_3C(O)O_2$ radical, Journal of Geophysical Research: Atmospheres, 103, 25 273–25 285, 1998.